Synergistic effect of a fluorinated azobenzene for transforming spherical micelles into thread-like micelles with a disk-like cross-section

Natalia Rincón-Londoño [a,d], Alberto S. Luviano [b], Antonio Tavera-Vázquez [c], Susana Figueroa-Gerstenmaier [b], Rolando Castillo [a,*]

[a] *Instituto de Física, Universidad Nacional Autónoma de México, P.O. Box 20-364, 01000 México City, Mexico*
[b] *Departamento de Ingenierías Química, Electrónica y Biomédica, División de Ciencias e Ingeniería, Universidad de Guanajuato, Campus León, León, Gto, Mexico*
[c] *Pritzker School of Molecular Engineering, The University of Chicago, Chicago, IL 60637, USA*
[d] *Departamento de Ingeniería Física, División de Ciencias e Ingenierías, Universidad de Guanajuato, Campus León, León, Gto, Mexico*

ARTICLE INFO

ABSTRACT

The free energy in solutions of amphiphilic molecules leads to the formation of supramolecular structures, often making spherical aggregates, worm-like micelles, vesicles, and lamellae. In this work, we add a fluorinated azobenzene, 4-(4-trifluoromethoxy phenyl azo) phenol (Azo-3F) to a solution mainly made of spherical and rodlike micelles of CetylTrimethylAmmonium Bromide (CTAB) and sodium salicylate (NaSal). These structures transform to disk-like micelles, which concatenate through hydrogen bridges to form long thread-like structures highly similar to worm-like micelle structures. This conclusion was reached after observing that NMR results suggest the formation of aggregates in solution with Azo-3F molecules inside them. Viscosity increases by three orders of magnitude at low shear rates when Azo-3F is added, and it shear-thins as the shear rate increases. The viscoelastic spectra show that the fluid changes from viscous to viscoelastic. Cole-Cole plots follow semicircles, typical of Maxwellian behavior below $\sim 35\,°C$. Cryo-TEM micrographs of the solution with Azo-3F show giant thread-like structures, and cross-sectional analysis of SAXS and WAXS profiles predict oblate ellipsoidal structures. In addition, MD simulations show that the disk-like micelles interact mainly through hydrogen bonds and electrostatics, forming micellar strings. These strings behave similarly to worm-like micelles, explaining why the solution behaves as a Maxwellian fluid at relatively low temperatures. Consequently, when some specific molecules are introduced in supramolecular structures, such as a spherical micelle, they can be transformed into disk-like micelles that assemble into thread-like micelles.

1. Introduction

In an aqueous medium, surfactants self-assemble in different morphologies. By minimizing the system's free energy, these supramolecular structures can be transformed and their shapes modified, which also introduces a change in the rheological behavior of the fluid where they are embedded [1–3]. Spherical, Worm-like Micelles (WLMs), vesicles, and lamellae are the most common aggregates with many important industrial applications [4,5]. According to the geometrical model, supramolecular structure morphology is a consequence of the geometry of the involved molecules in aggregation, characterized by a packing parameter [6,7], which can be modified through changes in surfactant concentration, temperature, or ionic strength of the medium, as it occurs when pH is modified, or through the use of different counterions or ionic

salt addition. Adding hydrophobic counterions (hydrotropes) or co-surfactants also modifies the assembly. In this way, the whole packing of the different entities included in the supramolecular self-assembly defines a spontaneous curvature whose modification has a free energy cost [6–8]. At concentrations above a first critical micelle concentration (CMC), surfactants are usually packed in spherical micelles, and these solutions usually follow a Newtonian behavior. When the CMC is exceeded, a sphere-cylinder transition can be achieved once the free energy is favorable. Cylindrical micelles can be long and flexible (WLMs), where the way to minimize the free energy is by decreasing the number of unfavorable hemisphere end-caps by increasing the lineal cylindrical section [9]. In this case, a large number of solutions with WLMs present a Maxwellian behavior $G(t) = G_o \exp(-t/\tau_R)$ at long times or equivalent, at low and intermediate frequencies, ω, in its related

complex modulus $G^*(\omega) = i\omega\, \widetilde{G}(\omega) = [G'(\omega) + i'G''(\omega)]$; although, there are well-known examples of WLMs not following that behavior [10,11]. The elastic modulus, G_o, and the relaxation time, τ_R, can be obtained from the linear viscoelastic spectrum from the crossing between the $G'(\omega)$ and $G''(\omega)$ curves. The formation of giant cylindrical micelles increases the solution's viscosity and introduces an elastic contribution to the rheological properties producing a viscoelastic fluid [12]. Both properties are due to the micellar network formed by the entanglement of these giant cylindrical micelles [13]. WLMs are of great interest due to their rheological properties with applications in the manufacturing of personal care, cleaning products, etc [14,15].

However, other structures, such as Disk-Like Micelles (DLMs), are not well known and relatively uncommon compared to spherical or WLMs [16–18]. The ladder model shows that the growth of DLM is governed by the difference between the standard chemical potentials of surfactant molecules in DLMs and WLMs, characterized by the parameter $p = (\widetilde{\mu}^{(C)} - \widetilde{\mu}^{(D)})/k_B T$; here, $\widetilde{\mu}^{(C)}$ and $\widetilde{\mu}^{(D)}$ are the standard chemical potentials of molecules in cylindrical and DLMs, respectively [16]. For $p < 0$, the formation of DLMs is energetically unfavorable, and surfactants form cylindrical micelles. In contrast, for $p > 0$, DLMs are formed. However, $p > 0$ corresponds to a positive excess of peripheral energy in the micelles, which increases as their diameter increases, limiting micellar growth. For this reason, DLMs can appear in a restricted concentration range and with small peripheral energies, where $0 < p < 0.1$. DLMs present a very low spontaneous curvature in the almost flat part of the disk, and a non-zero one at the edges, suggesting a different molecular composition in these two regions when the micelle is made of several entities. Some DLM systems present a rheological behavior similar to those with WLMs [16,18].

Disks are a unique form of stable surfactant self-assembly not commonly found in Nature, although some examples are mentioned in the literature. Zemb *et al.* found DLMs in mixtures of myristic acid and hydroxide-exchanged forms of cetyltrimethylammonium chloride [19], which at high dilution show small-angle neutron scattering (SANS) signals decreasing as the second power for low scattering vectors ($1 \times 10^{-3} < q < 1 \times 10^{-2}\,\text{Å}^{-1}$). The formation of disk-shaped micelles is also stimulated by adding small amounts of lauric acid to a micellar solution of sodium dodecyl sulfate and cocamidopropyl betaine [18]. This system presents a Maxwellian behavior just before a nematic transition. The authors assumed the formation of entangled, flexible, living columnar objects composed of packed DLMs in the isotropic phase. Sodium dodecyl sulfate in the presence of the counterion p-toluidine hydrochloride shows a sequence of phase transformations on increasing the counterion concentration: hexagonal, nematic, isotropic, nematic, lamella. WLMs form a nematic phase close to the hexagonal phase, and close to a lamellar phase are DLMs, suggesting a gradual prolate to oblate change in the aggregate morphology with increasing counterion concentration [17]. In a three-component solution composed of sodium lauryl ether sulfate, cocamidopropyl betaine, and dodecanoic acid, viscosity was found to pass through a maximum at a particular fatty acid concentration. Before that viscosity peak, spherical and short worm-like micelles transform into longer worms as the fatty acid concentration increases. At some point, after the viscosity peak, flat ribbonlike structures form as an intermediate state from worms to disks. Finally, the discoidal micelles become the dominant form of self-assembly at high enough fatty acid concentrations [16].

The main goal of this report is to present a study on a novel system that self-assembles in DLMs. As we will describe below, these DLMs are formed in a solution of spherical micelles made of Cetyl-TrimethylAmmonium Bromide (CTAB) and sodium salicylate (NaSal) when a hydrophobic fluorinated azobenzene is incorporated into the micellar structure; however, these structures are apparently not stable enough, and they concatenate to form thread-like structures in the overlapping regime, not observed before at the CTAB concentration and R = [NaSal]/[CTAB] used in this investigation. On the other hand, we

engineered this complex fluid to be prone to structural changes given the photosensitivity of the fluorinated azobenzene, 4-(4-trifluoromethoxy phenyl azo) phenol (Azo-3F), since it presents trans–cis isomerization under UV light. As we will see, Azo-3F incorporates into the spherical micelles of the original micellar system, giving rise to strong intermolecular interactions, as observed with Nuclear Magnetic Resonance (NMR) spectra, modifying the micellar structure. However, incorporating this azobenzene does not produce an intelligent fluid. Our group has previously investigated the effect of including photoswitchable molecules in WLMs solutions to produce intelligent fluids and the mechanisms that sometimes prevent chromophores from responding well to an external stimulus such as UV irradiation [20,21]. In the present paper, we show that the high hydrophobicity of the chromophore, due to its trifluoromethyl moiety, impacts the photoswitchable responses within the micelles. As pointed out by Lee and coworkers [22], it is imperative to combine different experimental techniques to characterize self-assembled materials. Otherwise, misleading results might be considered true. Here, besides the mentioned NMR spectra, we combine Molecular Dynamics (MD) simulations with real and reciprocal space imaging techniques to fully characterize the system's structure, which has a consequence in the rheological properties. MD suggests the concatenation of the newly formed discotic structures into thread-like structures. We observe these structures with Cryogenic Transmission Electron Microscopy (Cryo-TEM) and identify their cross-section by Small- and Wide-Angle X-ray Scattering (SAXS and WAXS). Therefore, the formation of thread-like structures explains the change in the rheological properties of the original micellar solution induced by the Azo-3F incorporation producing a Maxwellian fluid at low and intermediate frequencies, as shown later on. In summary, we designed a system in which some specific photoswitchable molecules are introduced in surfactant-supramolecular structures, such as spherical micelles, to transform them into disk-like micelles that concatenate to produce thread-like micelles. The different length-scale structures and rheological responses can improve their implementation for novel technologies.

2. Experimental section

2.1. Materials

CetylTrimethylAmmonium Bromide (CTAB, > 99%, Fluka, Switzerland), sodium salicylate (NaSal, 99.5%, Sigma-Aldrich, Canada). Reagents were used as received. 4-(4-trifluoromethoxy phenyl azo) phenol (Azo-3F) was synthesized following a method described elsewhere [23,24]. It was purified using 9:1 ethyl acetate in hexane as a diluent through column chromatography. ^{1}H NMR (500 MHz, TMS) of Azo-3F was measured in deuterated chloroform (CDCl$_3$, δ ~ 7.25 ppm), chemical shifts δ (ppm): 7.90 (4H, m, Ar-H), 7.33 (2H, d, Ar-H), 6.94 (2H, d, Ar-H), 5.50 (1H, s, Ar-OH). Samples were prepared with ultrapure deionized water (Nanopure, USA) and those for NMR with deuterated water (D$_2$O, 99%, Sigma-Aldrich).

2.2. Sample preparation

Azo-3F was suspended in water at a concentration of 10 mM ($C_{AZO} = 10$ mM), then CTAB was added. The suspension was stirred and heated up to 40 °C until full solubilization. Then, NaSal was added. The mixture was stirred for 24 h and left to relax for 48 h. Micellar solution ratio R = 0.33 (R = [NaSal]/[CTAB]) with [CTAB] = 60 mM. Another sample without Azo-3F was also prepared, following the same procedure, to be used as a reference for comparison.

2.3. Rheological measurements

Rheological measurements were performed with a MCR-702 Twin-Drive rheometer (Anton Paar, Austria). Flow curves and oscillatory

measurements were carried out in a cone-plate geometry (40 mm in diameter and 2° cone angle) with temperature control (± 0.1 °C). A solvent trap was used to avoid water evaporation. The oscillatory experiments were obtained in the linear regime.

2.4. ^{1}H NMR and ^{19}F NMR

^{1}H NMR and ^{19}F NMR spectra were acquired on a Bruker AVANCE III HD 500 MHz (USA) equipped with a 5-mm z-axis gradient BBFO probe at various temperatures. NMR experiments were recorded using standard Bruker pulse sequences. NMR spectra are referenced to the water signal resonance at each temperature; samples were dissolved in D_2O and deuterated chloroform.

2.5. SAXS and WAXS

The experimental setup is a SAXSLAB (XENOCS) Ganesha (Denmark) apparatus provided with a motorized collimation system consisting of a JJ X-Ray high precision 4-blade slits with single crystal low-scatter blades for SAXS and WAXS placed in a 3.9 m long evacuated camera (2.5×10^{-2} mbar), with a Pilatus 300 K solid-state photon-counting detector. The x-ray source is a microfocus Xenocs GeniX3D CuKα (λ = 1.5406 Å). The nominal measurement range for the scattering vector, q, is: $0.006 < q < 3$ Å^{-1}. Raw data were reduced using a SAXSGUI V2.19.02 implementation software (SAXLAB) and analyzed using the Igor Pro SANS software according to standard methods [25]. A non-diluted 200 μL sample was prepared in a quartz capillary (length = 80 mm, outer diameter = 1.5 mm, wall thickness = 0.01 mm) (Hampton Research, USA). A deionized water sample was used as background for the data reduction process. SAXS experiments were run for 13 h, and WAXS experiments for 5 h. All measurements were done at room temperature (25 °C).

2.6. Cryo-TEM

Samples were prepared for cryo-TEM imaging by application of 3.5 μL of sample onto plasma cleaned (Gatan Solarus) Quantifoil grids (1.2/1.3, copper 200 mesh; Electron Microscopy Sciences) and subsequently plunge freezing in liquid ethane using the Vitrobot Mark IV (Thermo Scientific). Grids were imaged on the Thermo Scientific Glacios (200 kV) with the Ceta-D camera using EPU software (Thermo Scientific). Grids were stored in liquid nitrogen until use. Control experiment samples were imaged on the Thermo Scientific Titan Krios 3Gi (300 kV) with the K3 direct detector (Gatan).

2.7. Molecular dynamics simulations

Molecular dynamics simulations were performed using the GROMOS force field 54a7 included in the GROMACS 2019 package [26,27]. The ATB server generated the molecules; the IDs for these are 603322 (Azo3F), 10929 (CTA$^+$), and 16917 (Sal$^-$) [28,29]. Ions were added after the system was solvated with the SPC/E water model [30]. The initial configuration was 600 CTAB and 200 NaSal molecules in a box of size $5 \times 5 \times 15$ nm^3, then the box was enlarged to $6.5 \times 6.5 \times 15$ nm^3, and 100 Azo3F molecules were added. This procedure was done to force a faster micelle formation. Finally, the box was enlarged to a size of $20 \times 20 \times 15$ nm^3, and it was filled with water molecules. Bromide and sodium ions were added to produce an uncharged system. Periodic boundary conditions were applied in every direction. The system was minimized using the steepest descent method and integrated using the leapfrog algorithm with 50,000 steps with 0.01 nm size. After minimization, 5 ns in (NVT) canonical ensemble with a V-rescale thermostat at 25 °C was performed. Data production was achieved under the isobaric-isothermic (NPT) ensemble during 2 μs using a V-rescale thermostat at 25 °C, with a Parrinello-Rahman barostat at 1 bar and compressibility of 4.5×10^{-5} bar^{-1}. The particle mesh Ewald method was used to calculate electrostatic interactions with a cut-off radius of 1.2 nm. For a more detailed and clear view of the structure, a small system with 273 CTAB, 91 NaSal, and 46 Azo-3F molecules in a box of $6 \times 6 \times 6$ nm^3 was used, afterward enlarged to a $14 \times 14 \times 14$ nm^3 box. In each configuration, R values and the ratio of Azo-3F/surfactant molecules are preserved as the experimental ones.

3. Results and discussion

3.1. Rheological behavior

Fig. 1a presents the viscosity, η, as a function of the shear rate, $\dot{\gamma}$, for the CTAB/NaSal micellar solution with $C_{AZO} = 0$ and $C_{AZO} = 10$ mM at 25 °C. Without Azo-3F, the viscosity of the solution is almost constant for two orders of magnitude in $\dot{\gamma}$, and with a small shear thinning at high $\dot{\gamma}$. This behavior corresponds to the micelles' alignment of CTAB/NaSal at R = 0.33, consistent with a mixture of spherical and rod-like micelles without entanglement (See Fig. SM4) [31–35]. However, when Azo-3F is added, the viscosity at low shear rates increases by three orders of magnitude (from 480 to 165,000 mPa s), and it shear thins as the shear rate increases. It seems as if the system CTAB/NaSal with Azo-3F produces self-assembled structures that align under flow, lowering the viscosity as the shear rate goes up. The inset of Fig. 1a presents the shear stress, σ vs. $\dot{\gamma}$ for the solutions under discussion. A sheet of light in the gradient-vorticity plane installed in a transparent Couette geometry showed a few shear-induced structures similar to those in WLM systems in the dilute regime (not shown) [36]. Fig. 1b presents viscoelastic spectra for the system with $C_{AZO} = 0$ and $C_{AZO} = 10$ mM at 25 °C. When Azo-3F is added to the CTAB/NaSal micelle solution, the fluid changes from a viscous to a viscoelastic one; for $C_{AZO} = 0$ mM, G' (ω) and G'' (ω) do not cross to each other, however, at $C_{AZO} = 10$ mM, the curves cross at a very low frequency (~0.0015 s^{-1}). As mentioned, the structure CTAB/NaSal at R = 0.33 is a mixture of spherical and tiny rod-like micelles without entanglement consistent with a viscous fluid. Fig. 1c presents the viscoelastic spectra of CTAB/NaSal with $C_{AZO} = 10$ mM as temperature increases and their corresponding Cole-Cole plots (inset Fig. 1c). As temperature increases, the viscoelastic spectra of the micellar solution with Azo-3F move up to higher frequencies, G_o decreases at small pace, and τ_R decreases two orders of magnitude when temperature changes from 25 °C to 45 °C. Cole-Cole plots follow semicircles, typical of Maxwellian behavior below 40 °C; at higher temperatures, curves deviate from the expected semicircles of Maxwellian behavior at intermediate and high frequencies. Other stress relaxation modes start to appear, or structures producing that behavior are destroyed. In summary, the flow curves and viscoelastic spectra suggest a change in the aggregate morphology of the solution due to the Azo-3F addition.

3.2. ^{1}H NMR and ^{19}F NMR

The most apparent reason for explaining why the rheological behavior of the CTAB/NaSal micelle solution (R = 0.33 and [CTAB] = 60 mM) is so dramatically modified when Azo-3F is added is a change in the micellar structure. This new structure should be hosting in some way Azo-3F to prevent it from being in the water, where it is almost insoluble. NMR can give us insight into how the Azo-3F is incorporated into the micellar structure. Fig. 2a shows the structure and assigned proton labeling for Azo-3F and NaSal used in the spectra description. Fig. 2b presents the ^{1}H NMR spectra of Azo-3F and CTAB/Azo-3F. The spectrum of Azo-3F is obtained in a chloroform solution. These signals only correspond to the trans isomer, as Lim *et al.* reported [23]. We observed several signals that do not appear in Fig. 2b because they are outside the figure range. CTAB signals of CTAB/Azo-3F spectrum in D_2O are between 3 and 0.8 ppm, protons corresponding to –CH$_2$- and –CH$_3$ are between 1.3 and 0.89 ppm, respectively, and the signal of N$^+$-(CH$_3$) protons appear at 3 ppm. Here, we observe that proton signals 1, 2, and 3
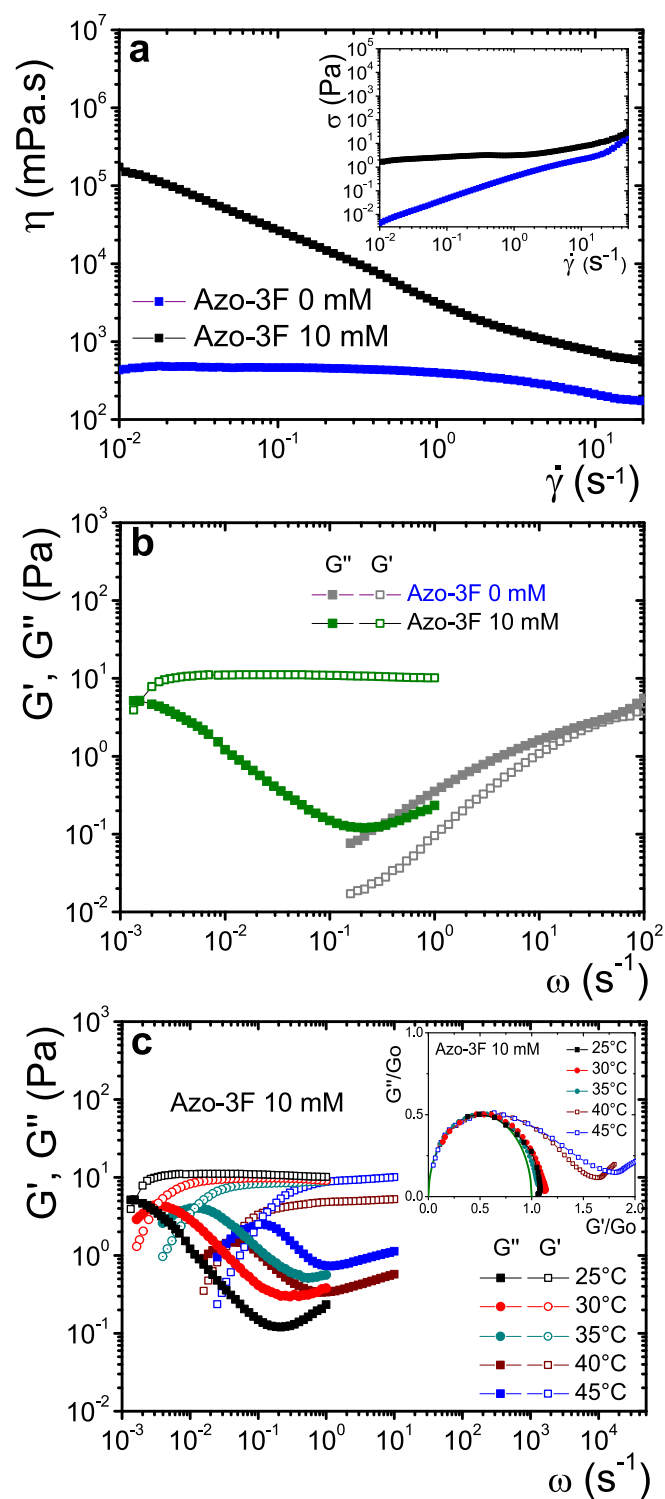
Fig. 1. a) viscosity (η) versus shear rate (γ̇) for CTAB/NaSal ([CTAB] = 60 mM, R = 0.33) varying C$_{AZO}$ = 0 and 10 mM at 25 °C. Inset: The corresponding shear stress (σ) versus shear rate (γ̇). G'(ω) and G''(ω) *vs.* ω for CTAB/NaSal ([CTAB] = 60 mM, R = 0.33) for C$_{AZO}$ = 0 mM and C$_{AZO}$ = 10 mM, at 25 °C in (b), and for C$_{AZO}$ = 10 mM at several temperatures in (c); the inset presents the Cole-Cole plots for each temperature in the main figure.

Fig. 2. a) structure and assigned proton labeling of Azo-3F (left) and NaSal (right). b)^{1}H NMR spectra of Azo-3F (10 mM) in CDCl$_3$ at 25 °C (simple signal at 7.28 ppm correspond to deuterated chloroform) and CTAB (60 mM)/Azo-3F (10 mM) in D$_2$O. Inset: Azo-3F (10 mM) in D$_2$O and CTAB (60 mM)/Azo-3F (10 mM) in D$_2$O. c) ^{1}H NMR spectra in D$_2$O of A) CTAB (60 mM)/NaSal (20 mM) at 25 °C, B) CTAB (60 mM)/Azo-3F (10 mM) at 25 °C. CTAB/NaSal/Azo-3F (10 mM) ([CTAB] = 60 mM, R = 0.33) at different temperatures: C) 25 °C, D) 30 °C, E) 50 °C, and F) 60 °C. The spectra use the water signal resonance as a reference for each temperature.

are shifted to lower chemical shifts (less electronegative or hydrophobic environments), and protons 4 are moved to higher chemical shifts (more electronegative or hydrophilic environments) compared with signals of Azo-3F in chloroform. These results suggest the formation of structures in solution where protons 1, 2, and 3 are inside the aggregates between
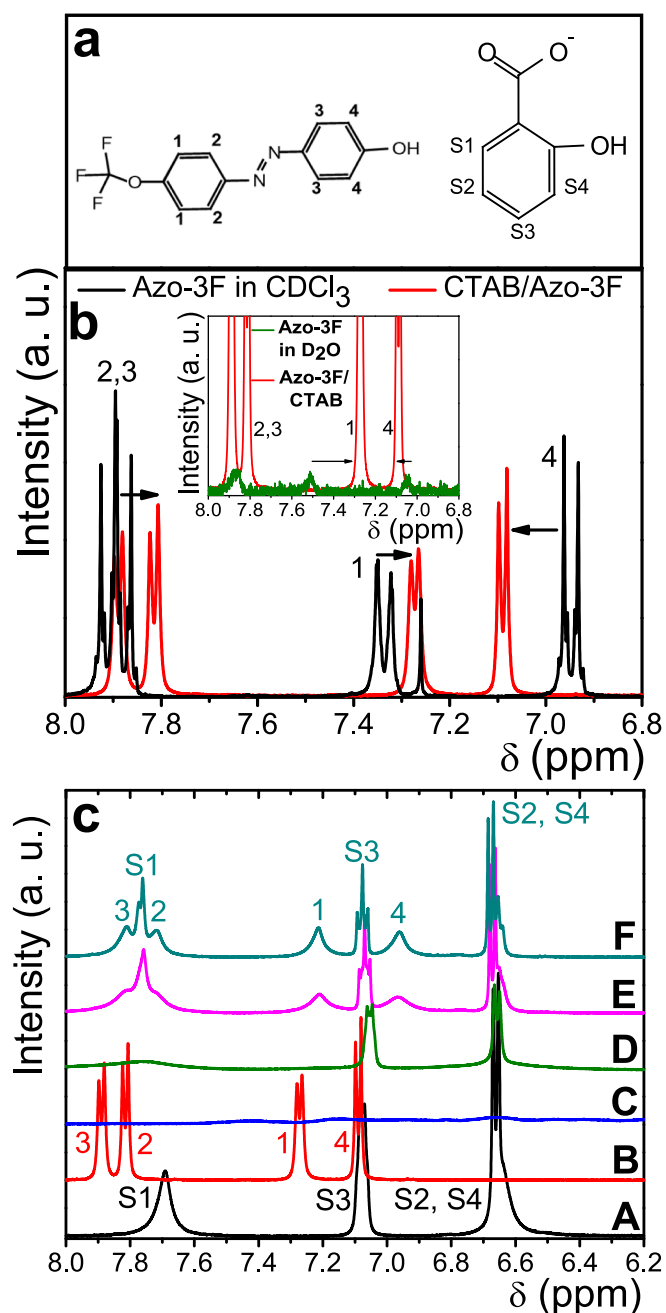
the surfactant tails, and protons 4 are close to the aggregate surface. Signals corresponding to protons 2 and 3 split into two signal groups, as observed with an azobenzene derivative inserted in a hydrophobic environment made of cyclodextrin [37]. For comparison, the inset of Fig. 2b presents the ^{1}H NMR spectra of Azo-3F and CTAB/Azo-3F in D$_2$O. Azo-3F signals have a small intensity due to the low solubility of this compound. Proton 1 signal moves to lower chemical shifts when Azo-3F mixes with CTAB, i.e., these proton moves to a more hydrophobic

environment. The same fact occurs when Azo-3F is incorporated into the aggregates formed in solution, where protons 1 are close to the surfactant tails. Fig. 2c presents the ^{1}H NMR spectra of CTAB/NaSal, CTAB/Azo-3F, and CTAB/NaSal/Azo-3F in D_2O. Spectrum (A) shows NaSal signals for proton labeling in Fig. 2a. Spectrum (B) corresponds to CTAB/Azo-3F, as shown in Fig. 2b. Spectra (C), (D), (E), and (F) correspond to CTAB/NaSal/Azo-3F system at 25, 30, 50, and 60 °C, respectively. Spectrum (C) does not present signals, probably due to low molecular mobility, indicating strong interactions or the formation of a very organized structure. The system has a higher viscosity at this concentration than the CTAB/NaSal system, as previously mentioned in Section 3.1. We increase the temperature of the solution to increase molecular mobility. At 30 °C, spectrum (D) presents some NaSal signals. Azo-3F signals begin to appear at 50 °C, as shown in (E). In (F), at 60 °C, the signals are more defined. In spectrum (F), proton signals for Azo-3F and NaSal are clearly observed. Azo-3F signals move to lower chemical shifts (less electronegative environments) compared to Azo-3F signals in (B). However, NaSal signals are almost not shifted with respect to the CTAB/NaSal spectrum (A), indicating that Azo-3F reflects an environmental change when NaSal is added to CTAB/Azo-3F.

In other ranges of chemical shifts (10–12 ppm), there are remarkable differences between spectra (C) at 25 °C and (D) at 30 °C, not shown in Fig. 2c, which are presented in Fig. SM2a. Here, CTAB/NaSal/Azo-3F spectra are shown as temperature increases from 25 °C to 29 °C. At 25 °C, the spectrum shows a double signal at ~ 12 ppm, which is attributed to hydrogen bonding, probably as a result of intermolecular interactions between the OH group of Azo-3F and the carboxyl group of NaSal, H-bonds between NaSal-NaSal, and intramolecular H-bonds in NaSal; the latter interaction is probably weaker due to electrostatic interaction with CTAB [38]. All those interactions fade away as temperature increases; at 30 °C, it is entirely lost. However, proton signals for NaSal appear more defined. At 29 °C, the spectrum does not present the hydrogen bonding signals, possibly due to the breaking of the hydrogen bridges, causing, at the same time, an increase in the NaSal mobility allowing NaSal signals to be observed with more definition. ^{19}F NMR spectra were also carried out to get some physical insight into the interactions involving fluorine in the CTAB/NaSal/Azo-3F solution. Fig. SM2b shows ^{19}F NMR spectra varying the temperature from 25 to 50 °C. Several peaks are observed at the lowest temperatures (25 °C and 26 °C). When the temperature reaches 28 °C, some peaks' intensity decreases while one increases, corresponding to a C-F bond that becomes a very well-defined singlet at 50 °C. These results suggest low mobility of Azo-3F at 25 °C, which sustains a strong interaction with other molecules that give rise to splitting the signal. However, interactions fade away when the temperature reaches 28 °C, and molecular mobility increases.

In summary, when Azo-3F is added to the micellar solution, it is incorporated into the original aggregate modifying it, forming a new self-assembled aggregate with strong interactions with both CTAB and NaSal. Although azobenzene presents a trans–cis isomerization under UV light, the CTAB/NaSal/Azo-3F mixture could be prone to be transformed through UV irradiation, inducing further changes in those newly formed aggregates through the isomerization of the azo compound. However, the isomerization rate from *cis*- to *trans*-isomer is accelerated in a polar medium [39]. Then, as the *cis* isomer is formed, it returns to the *trans*-isomer, and the structure of the new aggregates is not affected by UV irradiation. This issue is described in Fig. SM1.

3.3. SAXS-WAXS

We performed static scattering experiments to elucidate the self-assembled supramolecular structure formed after the Azo-3F addition to the spherical micelles. We measured the SAXS and WAXS patterns for CTAB/NaSal solution (C_{AZO} = 10 mM, R = 0.33 at 25 °C), which is in the semidilute regime. No further dilutions were made to determine the supramolecular structures in the solution, which produces the

rheological experiments described above. However, a scattered intensity profile with components of structure, S(q), and form, P(q), factors is indeed obtained; q is the scattering vector ($q=|q|$). To overcome this inconvenience, we focused on the scattering pattern obtained at the overlap between small and wide scattering vectors (0.004 < q < 0.4 Å^{-1}). In this interval, where P(q) plays a more relevant role, the observed structures represent individual portions of micelles and their cross-sectional size. Fig. 3a shows the x-rays scattering intensity pattern *vs.* the scattering vector q on the xy plane. An Oblate Core-Shell Ellipsoid model for the form factor was used to fit the intensity pattern to extract information from the size of the structures within the micelle [40,41]. The form factor is averaged over all possible orientations of the ellipsoid. The fitting can be observed as a red curve in Fig. 3a, spanning over the q interval 0.02–0.25 Å^{-1}. The overall description of the model is given by:

$$P(q) = background + \frac{scale}{V_{shell}} \int_0^1 |F(q, r_i, \alpha)|^2 d\alpha, \qquad (1)$$

where $F(q, r_i, \alpha) = 3(\rho_{core} - \rho_{shell})V_{core}j_1(u_{core})/3(\rho_{shell} - \rho_{solv})V_{shell}j_1(u_{shell})$ is the form factor for a core–shell spheroid with core semi-major and semi-minor axes $r_{maj,c}$ and $r_{min,c}$, respectively, and shell semi-major and semi-minor axes $r_{maj,s}$ and $r_{min,s}$, respectively (see Fig. 3b). $F(q, r_i, \alpha)$ is integrated over the orientation variable α, which is equal to the projection of the unitary vector in the direction of the spheroid's major axis and the average of the scattering vector q. Here ρ_{core}, ρ_{shell}, and ρ_{solv} are the scattering length densities of the core, shell, and solvent,
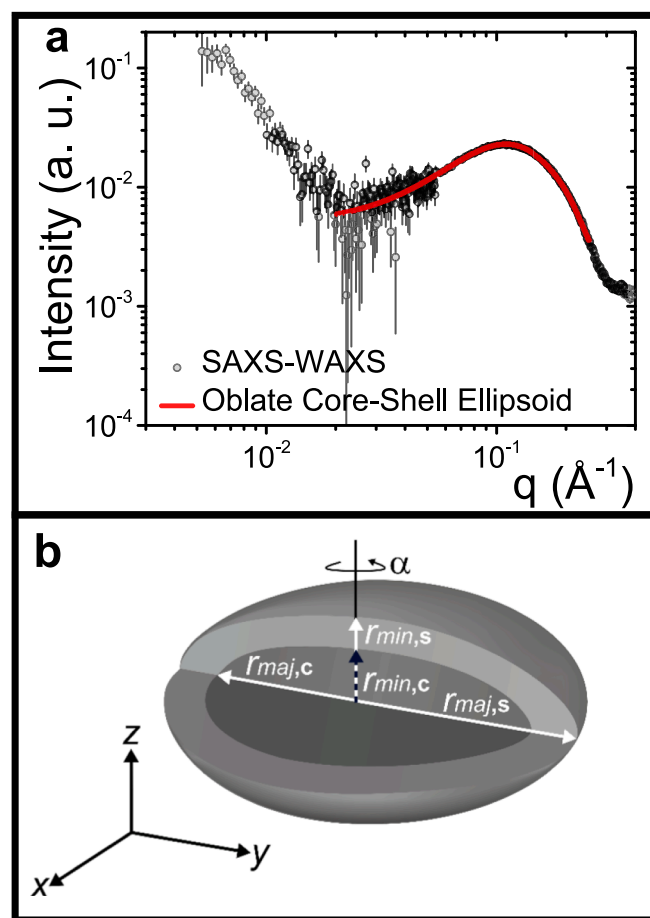

Fig. 3. a) saxs-waxs intensity pattern *vs.* q. The black open circles are the experimental results. The red curve represents an oblate core–shell ellipsoid model that fits the experimental curve over the q interval 0.02–0.25 Å^{-1}. b) Geometry of an oblate core–shell ellipsoid indicates the semiaxes considered by the applied model. The dashed arrow shows the size of $r_{min,c}$. α rotates around the z-axis.

respectively. V_{core} and V_{shell} are the volumes of the core and shell and are calculated as $V_{core} = (4\pi/3)r_{\min,c}r_{maj,c}^2$ and $V_{shell} = (4\pi/3)r_{\min,s}r_{maj,s}^2$ (see Fig. 3b). Additionally, j_1 is defined as $j_1(x) = (\sin x - x\cos x)/x^2$, with x defined as core and shell functions, $u_{core} = q\left[r_{maj,c}^2(1 - \alpha^2) + r_{\min,c}\alpha^2\right]^{1/2}$ and $u_{shell} = q\left[r_{maj,s}^2(1 - \alpha^2) + r_{\min,s}\alpha^2\right]^{1/2}$. Upon setting $\rho_{solv} = 9.47 \times 10^{-6}$ Å^{-2} for water, and the *scale* = 0.02 as the weight fraction of solids in the total sample suspension, the fit shows a good agreement with the experimental profile. The obtained values of the oblate ellipsoid's dimensions are summarized in Table 1. As we will see below, the size of these structures is close to those of micellar disks predicted with MD simulations. There is not enough data to obtain some information for q < 0.02 Å^{-2}.

3.4. Cryo-TEM

Micrographs in Fig. 4 show the supramolecular structures formed when Azo-3F is added to the micellar solution at different amplifications, which correspond to thread-like micelles whose total contour length is longer than 800 nm that is consistent with the high viscosity of the micellar system. For comparison, when Azo-3F is not added, see Fig. SM4. Therefore, from the cross-sectional scattering data analysis, the system presents structures with a discoidal cross-section, and from Cryo-TEM, we observe thread-like micelles, i.e., the system is made of worm-like micelles with a disk-like cross-section. This structure is confirmed with MD simulations.

3.5. Molecular dynamic simulation

MD simulations were performed to determine the most likely structure of the resulting aggregates after Azo-3F is added to the micelle solution. MD simulation of our experimental starting point, *i.e.*, CTAB/NaSal, with R = 0.33 produced, as expected, spherical micelles. The combined packing factors of CTAB and NaSal molecules and their intermolecular interaction produce mainly a solution of spherical micelles. These micelles interact through hydrogen bonds between NaSal molecules and electrostatic attraction among CTAB-NaSal. Spherical micellar solutions usually produce viscous Newtonian fluid, which co-incides with the behavior of the original CTAB-NaSal micellar solution shown above in Fig. 1a. If another type of molecule is incorporated into the micelles, the packing will be modified, and if the aggregate is stable, a structure change ensues.

Fig. 5a, 5b, and 5c present how the molecules involved in the micellar CTAB/NaSal/Azo-3F aggregate self-assemble as viewed from a side (the narrowest part of the disk) from a box of size $12 \times 12 \times 18$ nm^3. CTAB molecules (gray) are located in the flat region at the disk edge. The high number of CTAB molecules and their geometrical shape favor allocating them in a highly curved interface, which constitutes the disk edge. NaSal molecules (blue) are located in the flat region at the surface of the micelle, partially discharging that micellar region. Azo-3F molecules (red) in the same region are perpendicular to the micelle's flat part region, with their hydroxyls in contact with water molecules. The packing parameter of Azo-3F seems to be cylinder-like, mainly due to the location of the aromatic rings in the trans configuration. Embedding

Table 1
Structure values were calculated after fitting an oblate core–shell ellipsoid to the SAXS-WAXS intensity pattern. The uncertainty of the values corresponds to a standard deviation.

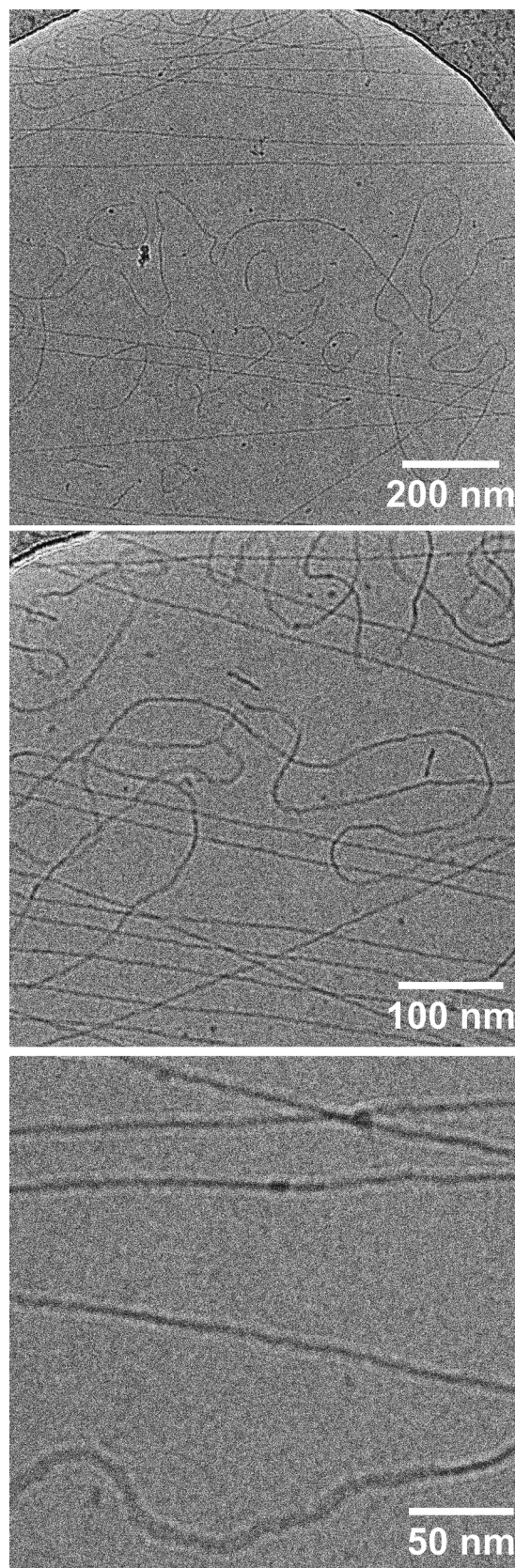| Oblate core–shell ellipsoid model				
	Semi-major core	semi-minor core	Semi-major shell	Semi-minor shell
Semiaxes (nm)	3.61 ± 0.06	0.81 ± 0.31	4.14 ± 0.06	2.96 ± 0.18

Fig. 4. Representative cryo-TEM micrographs at three different amplifications of a micellar solution of CTAB/NaSal ([CTAB] = 60 mM, R = 0.33) where Azo-3F was added (C$_{AZO}$ = 10 mM*).
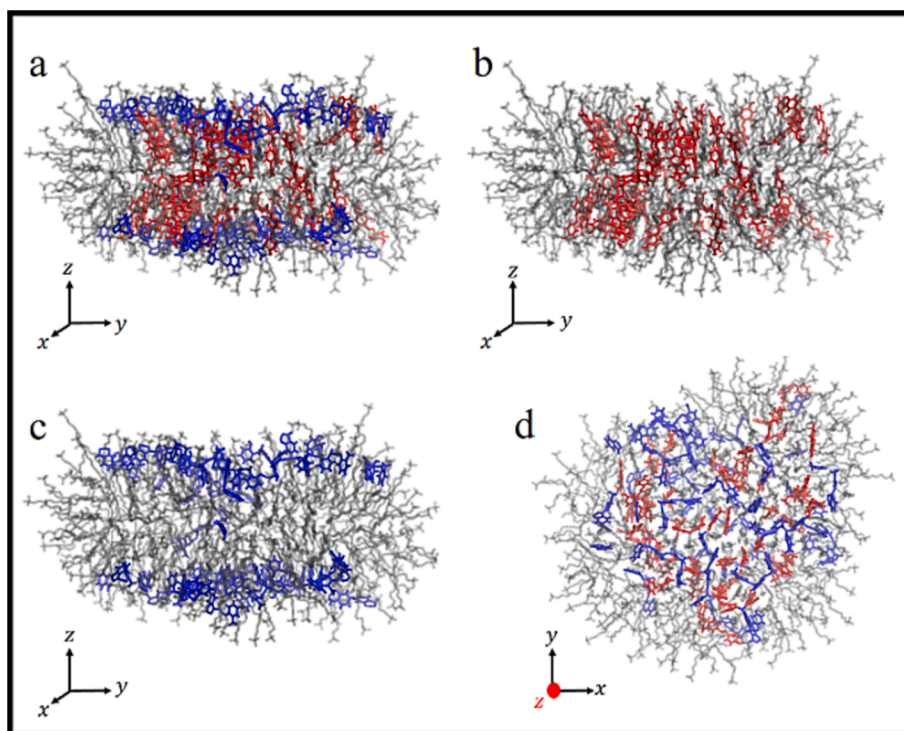
Fig. 5. a) disk-like micelle as viewed from its narrowest part, with the azo-3f (red), nasal (blue), and ctab (gray) molecules. b) The same as in (a), although NaSal molecules are not shown, allowing us to observe the Azo-3F molecules located perpendicularly to the flat part of the disk. c) The same as in (a), where the Azo-3F molecules are not shown, allowing us to observe the NaSal molecules at the surface of the micelle, mainly over the flat region. d) View of the disk flat region, where a homogeneous arrangement of NaSal and Azo-3F molecules is observed except at the disk rim.

these cylinder-like molecules induces the spherical micelle to form an oblate spheroid (b in Fig. 5). A view of the micelle from above, over the flat area of the disk, is shown in d of Fig. 5. Here, we observe a homogeneous arrangement of CTAB, NaSal, and Azo-3F except at the disk edge, where as mentioned above, there are primarily CTAB molecules. According to MD simulations, on average, the size of the micellar disk diameter is $\sim$ 8–10 nm, with a disk thickness of $\sim$ 4 nm, which is close to two CTAB molecular lengths.

Fig. 6 presents the CTAB headgroups number density *vs.* distance. Distance is evaluated by averaging distances from the Center-Of-Mass (COM) of all CH_3 at the CTAB tail tips, which are closest to the micelle center, to the center-of-mass of every CTAB headgroup near the micelle surface. Some examples of these distances are schematically shown in Fig. SM4. For comparison, calculations were done for spherical micelles and DLMs (Fig. 5). In Fig. 6, the number density profile for the spherical micelle presents a relatively sharp peak around 2 nm, which is close to the experimentally and simulated values for the radius of spherical and worm-like micelles made of CTAB/NaSal [9,42,43]. In contrast, the DLM number density profile is broader than in the spherical case. After the peak, the spherical number density profile drops sharply, but the disk-like one does it smoothly; the change in the number density
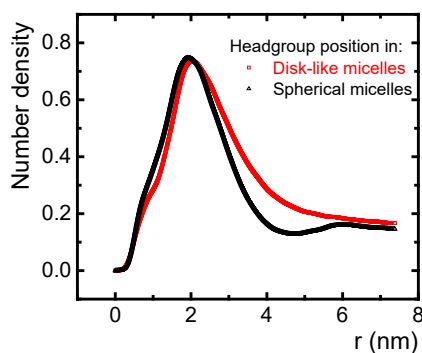
profiles results from the spherical micelles flattening upon Azo-3F embedding.

To appreciate how Azo-3F molecules are located inside the micelle disk, the fluorinated azobenzene is divided into five moieties, namely, O-CF$_3$, Ring-F, Nitrogens, Ring-OH, and OH. Fig. 7a presents the number density profiles of these moieties from the micelle center *vs.* distance. Distance is averaged from all CH_3 at the tail tip of CTAB molecules to the moieties of interest. Here, consecutive peaks of the mentioned pieces reveal the actual position of Azo-3F. The Azo-3F molecule, which has extremely low water solubility, has a hydrophilic moiety (OH), and the rest of it is quite hydrophobic (see Fig. 2a). This asymmetry, typical of amphiphilic molecules, is observed in the number density profiles of Fig. 7a, where the closest peak to the center of the micelle (r = 0 nm) corresponds to the COM of the O-CF$_3$. The farthest peak, at r = 1.8 nm, corresponds to the hydrophilic –OH moiety on the disk's flat surface. This value is close to the distance from the micelle center to the micellar surface in Fig. 6 for the polar CTAB group. The Azo-3F molecule places itself perpendicular to the flat region because its geometrical parameters fit better for the discotic structure of the micelle (see Fig. 7b).

Therefore, when a non-charged Azo-3F is added to the spherical micellar solution of CTAB/NaSal, fruitful interactions should occur to keep the newly formed micellar structure. Direct interactions of Azo-3F with NaSal are shown in Fig. 8a, where hydrogen bonds between the terminal OH of Azo-3F and COO$^-$ of NaSal are clearly observed, forming bridges between the carboxyl group of NaSal and the hydroxyl group of the Azo-3F. These results agree with the NMR experiments described in section 3.2 (Fig. SM2a). Simultaneously from our simulations, we can observe no interaction with the hydroxyl of NaSal attached to the aromatic ring, see Fig. 8b. Number density profiles of COO$^-$ and OH$^-$ of NaSal measured from the hydroxyl group of Azo-3F shows (Fig. 8c) that, on average, the NaSal hydroxyl terminal group is farther from the Azo-3F hydroxyl group than from the NaSal carboxyl group.

We have presented DLM formation as given by MD simulation. However, it is not expected that this kind of micelles dispersed in solution produces the viscoelastic behavior mentioned above; it would be similar to the spherical micelles in a low concentration regime. Nevertheless, our MD simulations also give a significant result. When the
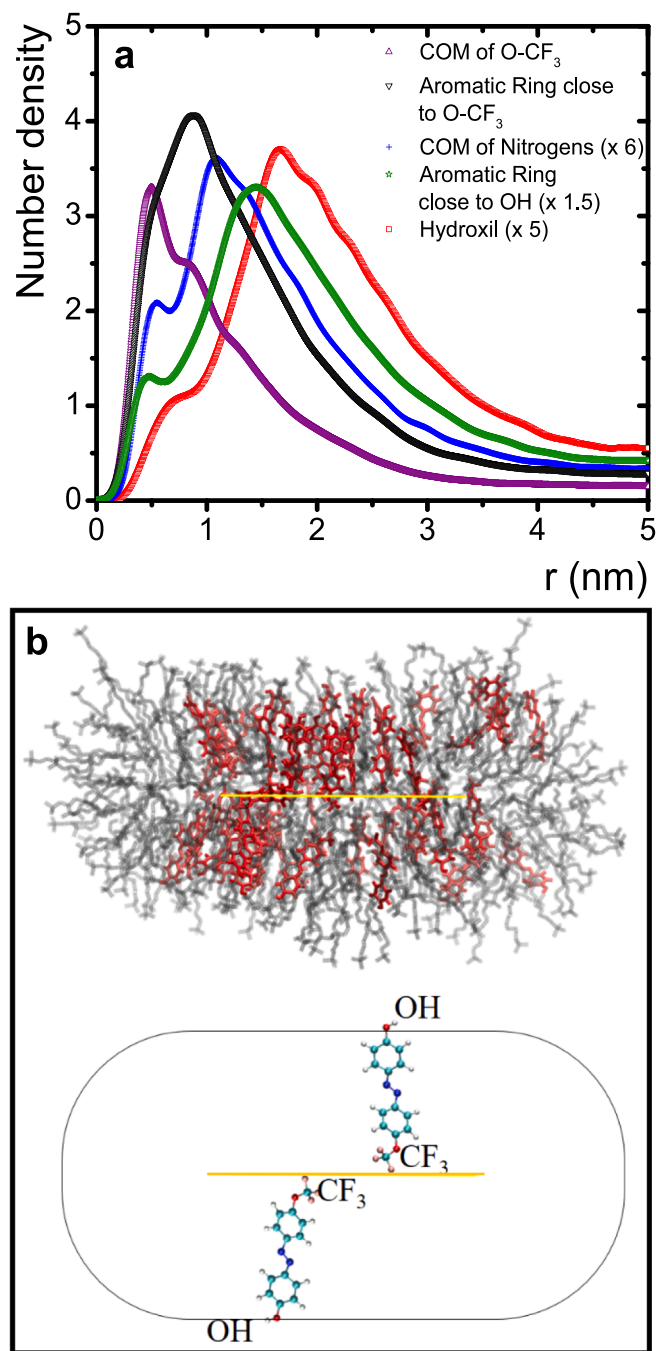

Fig. 6. Number density profiles of CTAB headgroups *vs.* distance for spherical and DLMs.

Fig. 7. a) Number density profiles for the Azo-3F moieties (see text). Azo-3F molecules are found only in the flat region of the micelle. They distribute from the micelle center in the following way: First, the COM of O-CF3; second, the adjacent aromatic ring; third, the COM of nitrogens; fourth, the aromatic ring closer to the hydroxyl; and finally, the hydroxyl. Some number density profiles are multiplied by a numerical factor to compare their peaks easily. b) The Azo-3F molecule places itself perpendicular to the flat region; its geometrical parameters fit better for the discotic structure of the micelle.

number of molecules increases, as in the box of size $20 \times 20 \times 15$ nm^3 (Fig. 9a), which shows the CTAB/NaSal/Azo-3F system, discotic micelles interact and form a DLM string; adjacent DLMs are tilted and slightly rotated from adjacent micelles (Fig. 9a and 9b). Although rotation is not entirely mandatory, tilt is mainly explained by the NaSal location in the flat region. This configuration allows hydrogen bridges among NaSal-NaSal and electrostatic interactions among NaSal and CTAB from adjacent micelles (Fig. 9c). These strings behave similarly to
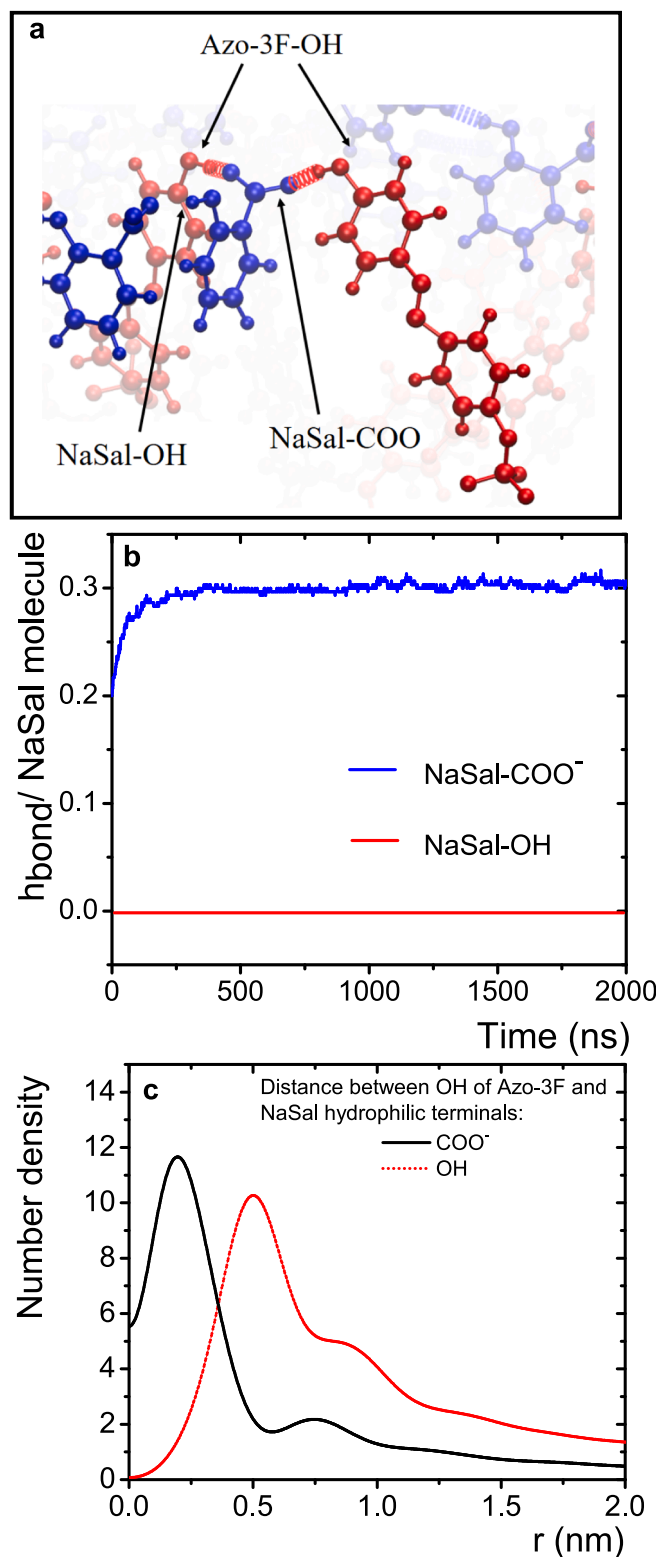

Fig. 8. a) Hydrogen bond interaction between OH of Azo-3F and COO$^-$ of NaSal. b) Average number of hydrogen bonds per molecule of NaSal (h$_{bond}$) with Azo-3F; essentially, the most crucial interaction is with COO$^-$ of NaSal. c) Average distances between OH of Azo-3F and NaSal hydrophilic terminals (COO$^-$ and OH).
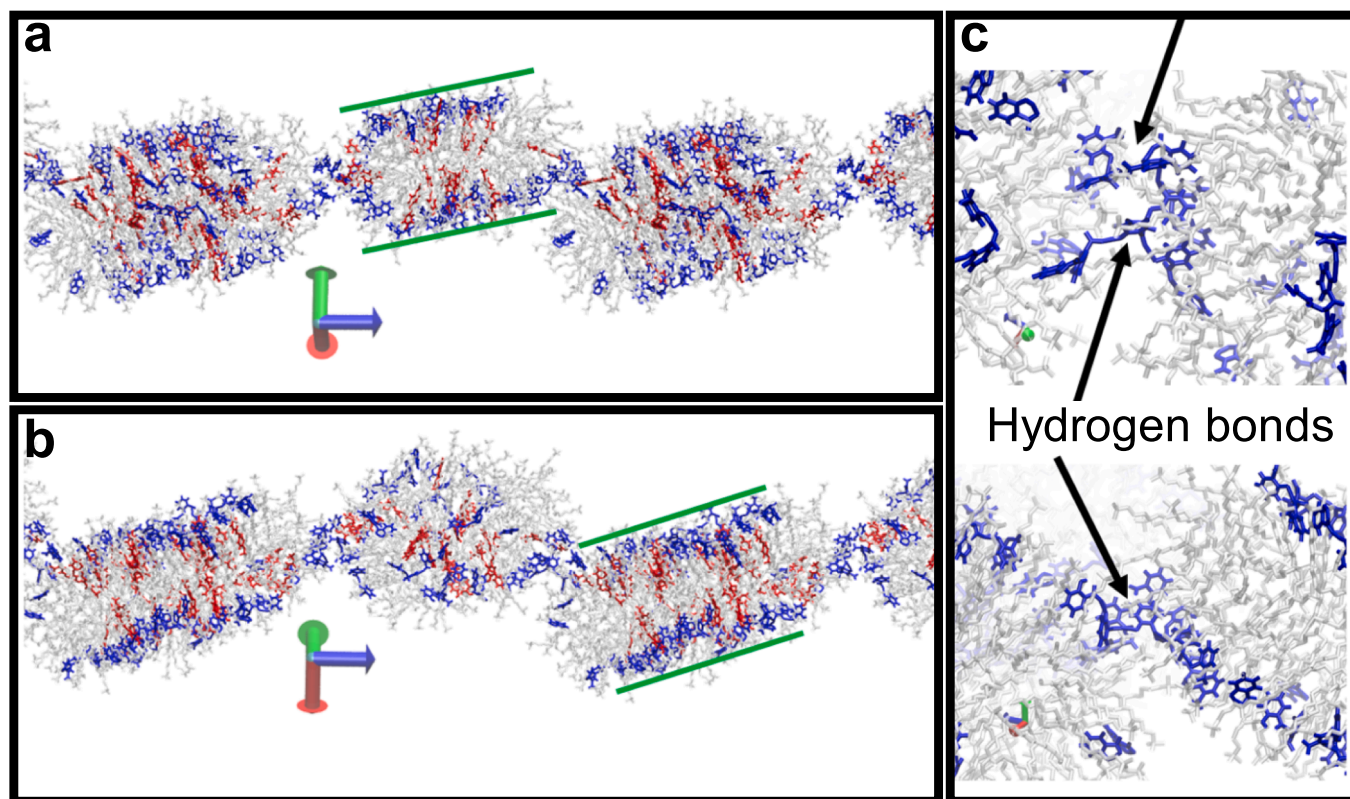
Fig. 9. a) interconnected disk-like micelles forming a supramolecular structure similar to a giant tubular micelle. b) Same images as (a) slightly rotated, as shown by the NaSal molecules (blue) in the flat region of the disks; CTAB (gray) and Azo-3F molecules (red). c) Intermicellar hydrogen bond interaction.

WLM, explaining why the solution behaves as a Maxwellian fluid at relatively low temperatures inducing a non-Newtonian (viscoelastic) behavior. However, as temperature increases (~*30–35 °C*), hydrogen bridges are destroyed, as shown by NMR (Fig. SM2a), and the Cole-Cole plots (Fig. 1c) confirm the loss of Maxwellian behavior.

4. Conclusion

From this study, we learned that when Azo-3F is added to the CTAB/NaSal micelle solution, the supramolecular structures mainly transform from spherical to disk-like micelles. There are just a few examples of this kind of micelles [16–18]. These micelles concatenate through hydrogen bridges to form long thread-like structures highly similar to worm-like micelle structures. The following facts support this conclusion: A) NMR results suggest the formation of aggregates in solution with Azo-3F molecules inside them; protons 1, 2, and 3 are inside the aggregates between the surfactant tails, and protons 4 are close to the aggregate surface. There are strong interactions among Azo-3F molecules and CTAB and NaSal within the aggregates. B) Without Azo-3F, the solution behavior is consistent with the micellar structure of CTAB/NaSal at R = 0.33, which is a mixture of spherical and rod-like micelles without entanglement. When Azo-3F is added, viscosity increases by three orders of magnitude at low shear rates, and it shears-thins as the shear rate increases; also, the viscoelastic spectra show that the fluid changes from a viscous to a viscoelastic one. Cole-Cole plots follow semicircles, typical of Maxwellian behavior below ~ 35 °C; at higher temperatures, curves deviate from the expected semicircles because other modes of stress relaxation start to appear, which is consistent with the breaking of a structure similar to those of WLMs due to the disk-like concatenation. C) Cross-sectional analysis of scattering patterns of the solution predicts oblate ellipsoid structures, which have a major axis of ~ 8.28 nm and a minor axis of ~ 5.92 nm. D) Cryo-TEM micrographs of the solution with Azo-3F show giant cylindrical micelles. E) MD simulations also confirm

that embedding Azo-3F into a spherical micelle induces the formation of an oblate spheroid, with an average diameter of ~ 8–10 nm and a disk thickness of ~ 4 nm. Azo-3F molecules are perpendicular to the flat part region of the micelle. In addition, MD simulations show that the disk-like micelles interact, forming micellar strings with these disk-like micelles. The interaction between disk-like micelles is mainly due to hydrogen bonds and electrostatics, which undoubtedly are weakened as temperature increases. These strings behave similarly to WLM, explaining why the solution behaves as a Maxwellian fluid at relatively low temperatures (< 35 °C).

This study shows how to transform supramolecular structures as spherical micelles into disk-like micelles that assemble into long thread-like micelles. Embedding relatively rigid cylinder-like molecules in a spherical micelle will induce the formation of oblate spheroids, which could be a guide to designing these uncommon aggregates. Another point that deserves a future study is determining the possible molecular configurations of aggregates that can be concatenated through hydrogen bonds to form strings with a rheological behavior like those of Maxwellian fluids (WLMs), with a very high viscosity, as we observed in this study.

CRediT authorship contribution statement

Natalia Rincón-Londoño: Investigation, Writing – original draft. **Alberto S. Luviano:** Investigation. **Antonio Tavera-Vázquez:** Investigation, Writiing - review & editing. **Susana Figueroa-Gerstenmaier:** Software. **Rolando Castillo:** Conceptualization, Funding acquisition,

Investigation, Writiing – review & editing.

Declaration of Competing Interest

The authors declare that they have no known competing financial interests or personal relationships that could have appeared to influence the work reported in this paper.

Data availability

No data was used for the research described in the article.

Acknowledgments

Appendix A. Supplementary material

Supplementary data to this article can be found online at https://doi.org/10.1016/j.molliq.2023.123066.

References

[1] D.P. Acharya, H. Kunieda, Worm-like micelles in mixed surfactant solutions, Adv. Colloid Interface Sci. 123–126 (2006) 401–413, https://doi.org/10.1016/j.cis.2006.05.024.

[2] C.A. Dreiss, Worm-like Micelles: An Introduction, in: C.A. Dreiss, Y. Feng (Eds.), Worm-like Micelles Adv. Syst. Characterisation Appl., 2017: pp. 1–8. 10.1039/9781782629788-00001.

[3] C.D. Umeasiegbu, V. Balakotaiah, R. Krishnamoorti, pH-Induced Re-entrant Microstructural Transitions in Cationic Surfactant-Hydrotrope Mixtures, Langmuir. 32 (2016) 655–663, https://doi.org/10.1021/acs.langmuir.5b02211.

[4] P. Sar, A. Ghosh, A. Scarso, B. Saha, Surfactant for better tomorrow: applied aspect of surfactant aggregates from laboratory to industry, Res. Chem. Intermed. 45 (2019) 6021–6041, https://doi.org/10.1007/s11164-019-04017-6.

[5] G. Tartaro, H. Mateos, D. Schirone, R. Angelico, G. Palazzo, Microemulsion Microstructure(s): A Tutorial Review, Nanomaterials. 10 (2020) 1657, https://doi.org/10.3390/nano10091657.

[6] J.N. Israelachvili, D.J. Mitchell, B.W. Ninham, Theory of self-assembly of hydrocarbon amphiphiles into micelles and bilayers, J. Chem. Soc. Faraday Trans. 2 (72) (1976) 1525, https://doi.org/10.1039/f29767201525.

[7] J. Israelachvili, Intermolecular and Surface Forces, Third Ed, Elsevier, 2011. 10.1016/C2009-0-21560-1.

[8] C.A. Dreiss, Worm-like micelles: where do we stand? Recent developments, linear rheology and scattering techniques, Soft Matter. 3 (2007) 956, https://doi.org/10.1039/b705775j.

[9] N.C. Das, H. Cao, H. Kaiser, G.T. Warren, J.R. Gladden, P.E. Sokol, Shape and Size of Highly Concentrated Micelles in CTAB/NaSal Solutions by Small Angle Neutron Scattering (SANS), Langmuir. 28 (2012) 11962–11968, https://doi.org/10.1021/la2022598.

[10] S.R. Raghavan, Y. Feng, Worm-like Micelles: Solutions, Gels, or Both?, in: C.A. Dreiss, Y. Feng (Eds.), Worm-like Micelles Adv. Syst. Characterisation Appl., 2017: pp. 9–30. 10.1039/9781782629788-00009.

[11] A. Tavera-Vázquez, B. Arenas-Gómez, C. Garza, Y. Liu, R. Castillo, Structure, rheology, and microrheology of worm-like micelles made of PB–PEO diblock copolymers, Soft Matter. 14 (2018) 7264–7276, https://doi.org/10.1039/C8SM01530A.

[12] B.A. Schubert, E.W. Kaler, N.J. Wagner, The Microstructure and Rheology of Mixed Cationic/Anionic Worm-like Micelles, Langmuir. 19 (2003) 4079–4089, https://doi.org/10.1021/la020821c.

[13] R.F. López-Santiago, J. Delgado, R. Castillo, Micellar entanglement and its relation to the elastic behavior of worm-like micelle fluids, J. Colloid Interface Sci. 626 (2022) 1015–1027, https://doi.org/10.1016/j.jcis.2022.07.003.

[14] J. Yang, Viscoelastic worm-like micelles and their applications, Curr. Opin. Colloid Interface Sci. 7 (2002) 276–281, https://doi.org/10.1016/S1359-0294(02)00071-7.

[15] S. Ezrahi, E. Tuval, A. Aserin, Properties, main applications and perspectives of worm micelles, Adv. Colloid Interface Sci. 128–130 (2006) 77–102, https://doi.org/10.1016/j.cis.2006.11.017.

[16] S.E. Anachkov, G.S. Georgieva, L. Abezgauz, D. Danino, P.A. Kralchevsky, Viscosity Peak due to Shape Transition from Worm-like to Disklike Micelles: Effect of Dodecanoic Acid, Langmuir. 34 (2018) 4897–4907, https://doi.org/10.1021/acs.langmuir.8b00421.

[17] S. Ghosh, V. Rathee, R. Krishnaswamy, V.A. Raghunathan, A.K. Sood, Re-entrant Phase Behavior of a Concentrated Anionic Surfactant System with Strongly Binding Counterions, Langmuir. 25 (2009) 8497–8506, https://doi.org/10.1021/la804330x.

[18] G. Colafemmina, R. Recchia, A.S. Ferrante, S. Amin, G. Palazzo, Lauric Acid-Induced Formation of a Lyotropic Nematic Phase of Disk-Shaped Micelles, J. Phys. Chem. B. 114 (2010) 7250–7260, https://doi.org/10.1021/jp1020774.

[19] T. Zemb, M. Dubois, B. Demé, T. Gulik-Krzywicki, Self-Assembly of Flat Nanodiscs in Salt-Free Catanionic Surfactant Solutions, Science (80-.). 283 (1999) 816–819. 10.1126/science.283.5403.816.

[20] N. Rincón-Londoño, C. Garza, N. Esturau-Escofet, A. Kozina, R. Castillo, Selective incorporation of one of the isomers of a photoswitchable molecule in worm-like micelles, Colloids Surfaces A Physicochem. Eng. Asp. 610 (2021), 125903, https://doi.org/10.1016/j.colsurfa.2020.125903.

[21] N. Rincón-Londoño, A. Tavera-Vázquez, C. Garza, N. Esturau-Escofet, A. Kozina, R. Castillo, Structural Changes in Wormlike Micelles on the Incorporation of Small Photoswitchable Molecules, J. Phys. Chem. B. 123 (2019) 9481–9490, https://doi.org/10.1021/acs.jpcb.9b07276.

[22] H.S. Lee, M. Adhimoolam Arunagirinathan, A. Vagias, S. Lee, J.R. Bellare, H.T. Davis, E.W. Kaler, A.V. McCormick, F.S. Bates, Almost Fooled Again: New Insights into Cesium Dodecyl Sulfate Micelle Structures, Langmuir. 30 (2014) 12743–12747, https://doi.org/10.1021/la502809y.

[23] H.S. Lim, J.T. Han, D. Kwak, M. Jin, K. Cho, Photoreversibly Switchable Superhydrophobic Surface with Erasable and Rewritable Pattern, J. Am. Chem. Soc. 128 (2006) 14458–14459, https://doi.org/10.1021/ja0655901.

[24] J.A. Tapia-Burgos, Synthesis and characterization of functionalized colloidal particles for self-assembling with controlled stimuli, UNAM (2017). http://132.248.9.195/ptd2017/marzo/0757387/Index.html.

[25] S.R. Kline, Reduction and analysis of SANS and USANS data using IGOR Pro, J. Appl. Crystallogr. 39 (2006) 895–900, https://doi.org/10.1107/S0021889806035059.

[26] G. development team M.J. Abraham, D. van der Spoel, E. Lindahl, B. Hess, GROMACS User Manual version 2019, 2019. http://www.gromacs.org.

[27] N. Schmid, A.P. Eichenberger, A. Choutko, S. Riniker, M. Winger, A.E. Mark, W.F. van Gunsteren, Definition and testing of the GROMOS force-field versions 54A7 and 54B7, Eur. Biophys. J. 40 (2011) 843–856, https://doi.org/10.1007/s00249-011-0700-9.

[28] H. Yan, Z. Han, K. Li, G. Li, X. Wei, Molecular Dynamics Simulation of the pH-Induced Structural Transitions in CTAB/NaSal Solution, Langmuir. 34 (2018) 351–358, https://doi.org/10.1021/acs.langmuir.7b03715.

[29] M. Stroet, B. Caron, K.M. Visscher, D.P. Geerke, A.K. Malde, A.E. Mark, Automated Topology Builder Version 3.0: Prediction of Solvation Free Enthalpies in Water and Hexane, J. Chem. Theory Comput. 14 (2018) 5834–5845, https://doi.org/10.1021/acs.jctc.8b00768.

[30] H.J.C. Berendsen, J.R. Grigera, T.P. Straatsma, The missing term in effective pair potentials, J. Phys. Chem. 91 (1987) 6269–6271, https://doi.org/10.1021/j100308a038.

[31] T. Shikata, H. Hirata, T. Kotaka, Micelle formation of detergent molecules in aqueous media: viscoelastic properties of aqueous cetyltrimethylammonium bromide solutions, Langmuir. 3 (1987) 1081–1086, https://doi.org/10.1021/la00078a035.

[32] T. Shikata, H. Hirata, T. Kotaka, Micelle formation of detergent molecules in aqueous media. 3. Viscoelastic properties of aqueous cetyltrimethylammonium bromide-salicylic acid solutions, Langmuir. 5 (1989) 398–405, https://doi.org/10.1021/la00086a020.

[33] Z. Lin, J.J. Cai, L.E. Scriven, H.T. Davis, Spherical-to-Wormlike Micelle Transition in CTAB Solutions, J. Phys. Chem. 98 (1994) 5984–5993, https://doi.org/10.1021/j100074a027.

[34] W.-J. Kim, S.-M. Yang, Effects of Sodium Salicylate on the Microstructure of an Aqueous Micellar Solution and Its Rheological Responses, J. Colloid Interface Sci. 232 (2000) 225–234, https://doi.org/10.1006/jcis.2000.7207.

[35] M. Vasudevan, A. Shen, B. Khomami, R. Sureshkumar, Self-similar shear thickening behavior in CTAB/NaSal surfactant solutions, J. Rheol. (N. Y. N. Y). 52 (2008) 527–550, https://doi.org/10.1122/1.2833594.

[36] J. Delgado, R. Castillo, Shear-induced structures formed during thixotropic loops in dilute worm-micelle solutions, J. Colloid Interface Sci. 312 (2007) 481–488, https://doi.org/10.1016/j.jcis.2007.03.010.

[37] J. Wang, Q. Li, S. Yi, X. Chen, Visible-light/temperature dual-responsive hydrogel constructed by α-cyclodextrin and an azobenzene linked surfactant, Soft Matter. 13 (2017) 6490–6498, https://doi.org/10.1039/C7SM01528C.

[38] L. Zhao, H. Zhang, W. Wang, G. Wang, Effects of sodium salicylate on didecyldimethylammonium formate properties and aggregation behaviors, J. Mol. Liq. 225 (2017) 897–902, https://doi.org/10.1016/j.molliq.2016.11.019.

[39] J. García-Amorós, D. Velasco, Recent advances towards azobenzene-based light-driven real-time information-transmitting materials, Beilstein J. Org. Chem. 8 (2012) 1003–1017, https://doi.org/10.3762/bjoc.8.113.

[40] M. Kotlarchyk, S. Chen, Analysis of small angle neutron scattering spectra from polydisperse interacting colloids, J. Chem. Phys. 79 (1983) 2461–2469, https://doi.org/10.1063/1.446055.

[41] S.S. Berr, Solvent isotope effects on alkytrimethylammonium bromide micelles as a function of alkyl chain length, J. Phys. Chem. 91 (1987) 4760–4765, https://doi.org/10.1021/j100302a024.

[42] C.N. Lam, C. Do, Y. Wang, G.-R. Huang, W.-R. Chen, Structural properties of the evolution of CTAB/NaSal micelles investigated by SANS and rheometry, Phys. Chem. Chem. Phys. 21 (2019) 18346–18351, https://doi.org/10.1039/C9CP02868D.

[43] A.S. Luviano, S. Figueroa-Gerstenmaier, E. Sarmiento-Gómez, N. Rincón-Londoño, Non-disruptive Mixing of Cyclodextrins and Worm-like Micelles in the non-dilute regime, J. Mol. Liq. 369 (2023), 120844, https://doi.org/10.1016/j.molliq.2022.120844.